mater.scichina.com link.springer.com

Published online 17 January 2024 | https://doi.org/10.1007/s40843-023-2711-x
Sci China Mater 2024, 67(2): 619–628

Orbital elasticity control of phase diagram for $La_{0.67}Sr_{0.33}MnO_3$ films

Ang Gao[1], Qinghua Zhang[2*], Zhuohui Liu[2], Fanqi Meng[3], Tongtong Shang[3], Hao Ni[4], Heyi Huang[2], Jianyu Du[2], Xinyan Li[2], Botao Yu[1], Dong Su[2], Kuijuan Jin[2], Chen Ge[2], Yanzhou Ji[5], Bo Wang[5], Qian Yu[6*], Ze Zhang[6], Longqing Chen[5*], Lin Gu[1*] and Cewen Nan[3]

ABSTRACT Transition metal oxides display rich functionalities, but intricate internal degrees of freedom pose a challenge to understanding phase diagrams as a road map for material exploration. Here, the order of orbital energy level (ELO) as a physical principle of phase diagrams is introduced and demonstrated to be effective by employing $La_{0.67}Sr_{0.33}MnO_3$ (LSMO) oxides. A phase diagram of LSMO associated with the oxygen content and strain is built combining DFT calculations and experiments, in which the structural stability is closely related to ELO. We thereby find a new phase with four-fold oxygen ordering as a result of ELO evolution. More important, orbital elasticity law, describing the degree of orbital splitting, is proposed to clarify the origin of ELO evolution, with the objective of design of functional oxides with specific functionality. This work broadens the means of performance modulation in the field of materials science and opens up an opportunity for phase diagram prediction from an orbital perspective.

Keywords: phase diagram, orbital energy level, orbital elasticity law, structural design, $La_{0.67}Sr_{0.33}MnO_3$ films

INTRODUCTION

Phase diagram, a graphical representation that describes the equilibrium relationship between phases, serves as a road map for material design and process optimization since it is the starting point for manipulating processing variables to achieve the desired microstructures [1–3]. Transition metal (TM) oxides have become pervasive and important functional materials due to their desirable properties, such as optical, electrical, magnetic, piezoelectric, ferroelectric, and thermoelectric properties [4–6]. The active d or f orbital degrees of freedom in TM oxides generate a rich phase diagram including a wide variety of structural or functional phases [7]. However, there are numerous types of structural transitions in the above oxides, and the true microscopic origin of these behaviors is rarely reported. It is challenging to predict a phase transition of TM oxides when subjected to changes in the external environment, or drawing phase diagrams. Modern *ab initio* calculations can provide this information [8], but the simple physics of these transitions often remains obscure. Orbital-related physics has attracted growing interest in functional materials research [9], trying to explain the origin of complex phase diagrams. The essential point is to seek a simple principle at the orbital level clarifying complicated phenomena in the structure-function relationship, which opens the door to a new stage in orbital physics.

The electron orbitals are believed to have important implications for the macroscopic functional properties of function materials [10,11]. The energy level of electrons, an important parameter of the orbital, is closely related to the interaction between atoms, influencing the orbital distribution and relative electronic occupation and hence the materials' properties. In VO_2 thin films, the metal-insulator transition temperature and the structural distortion depend on the orbital occupancy in the metallic state controlled by the strain-induced energy level change [12]. In FePc–SnTe system, ferroelectric order is coupled with the evolution of energy levels and electron transfer between d orbitals of the Fe atom [13]. The study [14] on carbon-based molecular junctions suggests that the properties of photocurrent depend directly on the relative positions of the frontier orbitals and the Fermi energy (E_F) of the electrode, revealing how molecular structure and orbital energies control electronic behavior. Bernhard's group [15] reported long-ranged Cu-based order with dz^2 orbital character at a $YBa_2Cu_3O_7$/manganite interface, providing new insight on the relation between superconductivity and charge order in the cuprates. In $LaSrCrO_3/LaSrMnO_3$ heterostructures, the strains distort the octahedron and trigger the e_g orbital splitting, which leads to the preferential occupation of the Mn x^2-y^2 (in-plane) d orbitals for tensile strain and z^2 (out-of-plane) orbitals under compressive strain, further leading to competition between ferromagnetic (FM) and antiferromagnetic (AFM) exchange interactions [16]. In conclusion, orbital energy levels (ELOs) are ubiquitously present in various aspects of material functionalities, including FM [17], ferroelectricity [18,19], superconductivity [15,20], and

[1] Beijing National Center for Electron Microscopy and Laboratory of Advanced Materials, School of Materials Science and Engineering, Tsinghua University, Beijing 100084, China
[2] Beijing National Laboratory for Condensed Matter Physics, Institute of Physics, Chinese Academy of Sciences, Beijing 100190, China
[3] State Key of Laboratory of New Ceramics and Fine Processing, School of Materials Science and Engineering, Tsinghua University, Beijing 100084, China
[4] College of Science, China University of Petroleum (East China), Qingdao 266580, China
[5] Materials Research Institute and Department of Materials Science and Engineering, The Pennsylvania State University, University Park, PA, 16802 USA
[6] School of Materials Science and Engineering, Zhejiang University, Hangzhou 312227, China
* Corresponding authors (emails: zqh@iphy.ac.cn (Zhang Q); yu_qian@zju.edu.cn (Yu Q); lqc3@psu.edu (Chen L); lingu@mail.tsinghua.edu.cn (Gu L))

energy storage and conversion [21]. Thus, a crucial step toward controlling material properties is exploring a general law of ELO distribution, which can be regarded as a promising starting point for insight into phase diagrams in materials science.

Here, we focus on the evolution of order of ELO in different crystal fields and strains to hunt for the nature of ELOs, achieving the purpose of structural prediction and phase diagram drawing on this basis. The perovskite (PV) manganite $La_{0.67}Sr_{0.33}MnO_3$ (LSMO) exhibits fascinating orbital characteristics and has been intensively studied [22–24], which provides us with a good platform to understand ELO. The crystal field and strain are used as effective tools to manipulate ELO in the LSMO system. A phase diagram of LSMO oxides regarding the oxygen content and strain is built through theoretical calculation, in which the phase transition is closely related to ELO evolution. We thereby find a new phase with four-fold oxygen ordering in the compressive regime. The phase diagram is confirmed by *in situ* scanning transmission electron microscopy (STEM). Based on this, we discover the orbital elasticity law that describes the degree of orbital splitting to guide the design of LSMO-like oxides with specific functionality.

EXPERIMENTAL SECTION

Calculation details

All first-principles calculations were performed with the Vienna *Ab Initio* Simulation Package (VASP) [25–27] based on density functional theory (DFT). Projector augmented wave [28] potentials were used to deal with the electronic exchange–correlation interaction along with the generalized gradient approximation (GGA) functional in the parameterization of the Perdew–Burke–Ernzerhof pseudopotential [29]. A plane wave representation for the wave function with a cutoff energy of 500 eV was applied. Geometry optimizations were performed using a conjugate gradient minimization until all the forces acting on the ions were less than 0.01 eV $Å^{-1}$ per atom. The *K*-point mesh with a spacing of ca. 0.03 $Å^{-1}$ was adopted. The crystal structures were built using VESTA software [30]. The LSMO structure with a 2 × 2 × 4 supercell containing 80 atoms or a 2 × 2 × 8 supercell containing 160 atoms were adopted for thermodynamic optimization.

Film preparation

The PV LSMO thin films with a thickness of ~20 nm were epitaxially grown on (001) $SrTiO_3$ (STO) and (001) $LaAlO_3$ (LAO) substrates (MTI Ltd.) using pulsed laser deposition (PLD) with a 308 nm XeCl excimer laser, an energy density of ~2 J cm^{-2}, and a repletion rate of 2 Hz. LSMO films were deposited at 680°C in a flowing oxygen atmosphere of oxygen pressure 1 × 10^{-3} Pa and cooled down to room temperature at 30°C min^{-1}. The deposition rate and the thickness of LSMO films were further calibrated by X-ray reflection.

In-situ characterization

The TEM sample was prepared by using focused ion beam (FIB) milling. Cross-sectional lamellas were thinned down to 100 nm thick at an accelerating voltage of 30 kV with a decreasing current from the maximum 2.5 nA, followed by fine polish at an accelerating voltage of 2 kV with a small current of 40 pA. Next, we fixed the thin cross-sectional TEM lamella on the heating chip by Pt deposition in the FIB system. The *in-situ* heating experiments were performed using a heating & bias DH30 holder produced by DENSsolutions. The atomic structures were investigated using the STEM (JEOL ARM-200CF) equipped with double spherical aberration (Cs) correctors, and electron energy loss spectroscopy (EELS) measurements were carried out using a Gatan spectrometer attached to the TEM in the STEM mode. High-angle annular dark field (HAADF) images were acquired at the acceptance angles of 68–260 mrad.

Physical properties measurement

The transport and magnetic properties of LSMO thin films were measured using physical properties measurement system (PPMS, Quantum Design Inc.). The temperature-dependent magnetization (*M*-*T*) was measured using field cooling mode with a magnetic field of 0.1 T, and the magnetic field was applied along the in-plane direction of the film. The X-ray diffraction (XRD) patterns of LSMO films were characterized by a high-resolution four-circle X-ray diffractometer instrument (Rigaku, Smartlab). X-ray absorption spectroscopy (XAS) of manganese L-edges and oxygen K-edges was measured under high-vacuum level 6 × 10^{-7} Torr (1 Torr = 133.3 Pa) in synchrotron radiation facilities.

RESULTS

Order of ELO

Taking the 3d orbital as an example, an isolated TM atom or ion with full spherical symmetry, and five d levels (d*xy*, d*xz*, d*yz*, dx^2-y^2 and dz^2) with $l = 2$ are degenerate. A particular orbital has a very specific direction in space as illustrated in Fig. 1a. When a TM ion is put in a solid, this degeneracy is lifted because of the interactions with the surroundings (Fig. 1b), mainly with nearest-neighbor ligands, e.g., oxygen, sulfur, and chlorine. The most typical situation is six-fold coordination: a TM ion in a ligand octahedron. In this case, the five-fold degenerate d levels are split into a lower-lying t_{2g} triplet (d*xy*, d*xz*, d*yz*) and a higher-lying e_g doublet (dx^2-y^2 and dz^2). The contrary is the case in tetrahedral coordination. A higher-lying t_{2g} triplet and a lower-lying e_g doublet are found. In pentahedral coordination, the degenerate t_{2g} triplet and e_g doublet further split, respectively, as shown in Fig. 1b. Apparently, the degenerate 3d orbitals generate an energy difference due to the effect of crystal field. This order, ELO, is defined as the following number series,

$$\mathrm{ELO} = \mathrm{arr}\{[1\mathrm{d}m\ 2\mathrm{d}m \ldots n\mathrm{d}m]\}, \quad (1)$$

where nd_m represents the 3d orbital; *n* is the sequence number of ions; *m* is the sequence number of the 3d orbital, which can be 1, 2, 3, 4, and 5; the operator of "arr" arranges the elements (nd_m) of the number series in order of the value (ELO) from the lowest to the highest.

The degree of orbital splitting is affected by the strength of the crystal field [31]. Meanwhile, strain also plays a key role in manipulating ELOs [16]. Hooke's law states that a spring undergoes an elastic deformation where the spring force is directly proportional to the elongation of the spring (Fig. 1c). And the proportionality coefficient (k) is the elasticity coefficient of a substance, which is determined only by the nature of the material. Analogous to Hooke's law, a specific crystal field is assumed to have an elastic coefficient for orbital splitting, which describes the degree of orbital splitting when subjected to strains (Fig. 1c). ELO is modulated based on the mastery of orbital splitting in crystal fields, with the objective of eventually

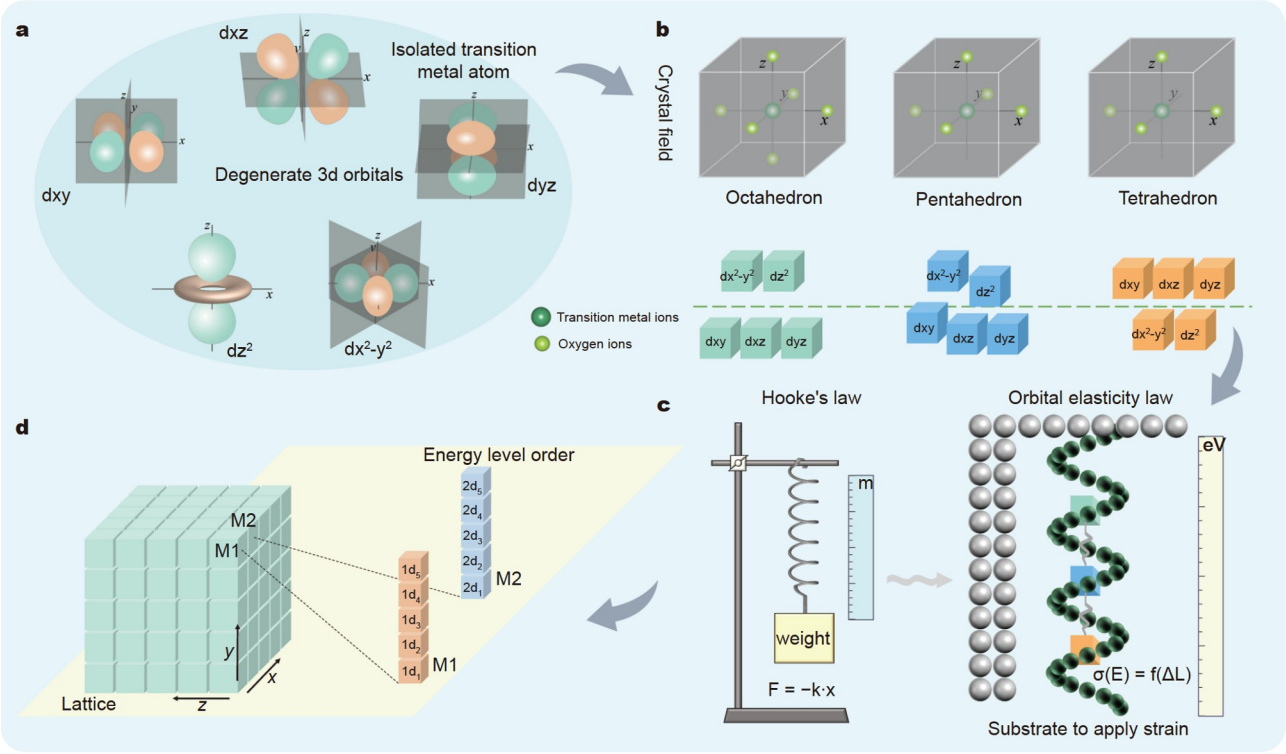

Figure 1 Scheme of controlling order of ELO. (a) Sketch of degenerate 3d orbitals (d*xy*, d*xz*, d*yz*, dx^2-y^2, and dz^2) for an isolated TM atom. (b) 3d orbital splitting states under different crystal fields, including regular octahedral, pentahedral, and tetrahedral crystal fields. Dark and light green spheres represent TM and oxygen ions, respectively. (c) Orbital elasticity law that describes the degree of orbital splitting with strains, analogous to Hooke's law that describes the relationship between stress and strain in materials. (d) Schematic diagram of ELO.

designing functional oxides (Fig. 1d).

LSMO structure design

In the PV-LSMO structure, the oxygen ions and the larger La/Sr ions form face-centered cubic packing, while the smaller Mn ions occupy the octahedral void. Fig. 2a shows the optimized structure with a unit cell (2 × 2 × 4) and an HAADF image of PV-LSMO. The sites of the doped Sr ions in the LSMO structure are filtered by supercell software [32], as illustrated by the pink ball in Fig. S1. Brownmillerite $La_{0.67}Sr_{0.33}MnO_{2.5}$ (BM-LSMO) is a prototype oxygen-deficient material that can be obtained from the PV-structured framework by removing half the oxygen ions from alternating MnO_2 layers (Fig. 2b). The BM-LSMO structure is characterized by layers of MnO_6 octahedra and MnO_4 tetrahedra stacked in an alternating fashion along the *c* axis. In this work, the oxygen contents (*x*) in our calculated phase diagram are distributed between those of the PV and BM phases, i.e., $2.5 \leq x \leq 3.0$.

Numerous studies have shown that Vo is mainly distributed along the in-plane direction in PV-LSMO films with in-plane strain [22,33,34]. Based on the PV-structural feature, Fig. 2c illustrates the possible phases including oxygen ordering and magnetic structure at different oxygen contents (*x*) of the $La_{0.67}Sr_{0.33}MnO_x$ structure. For $x = 3.0$, Mn ions coordinate with six oxygen ions to form MnO_6 octahedra as denoted by the green hexagon in Fig. 2c. The magnetic structure has FM order [35], as illustrated by the white arrow. The structure with $x = 3.0$ is denoted as Oct-FM. For $x = 2.875$, a quarter of the MnO_6 octahedra transform to MnO_5 pentahedra (blue pentagon) accompanied by in-plane ordered Vo with 4*c* periodicity along the *c* axis. Note that 4*c* periodicity refers to an in-plane Vo stripe every four layers along the *c* axis. Two kinds of magnetic structures, with FM and AFM orders, are considered for MnO_5 pentahedron layer, denoted as 4*c*-Pen-FM and 4*c*-Pen-AFM. For $x = 2.75$, one half of the MnO_6 octahedra transform to MnO_5 pentahedra, corresponding to ordered Vo with 2*c* periodicity. Two kinds of magnetic structures are marked as 2*c*-Pen-FM and 2*c*-Pen-AFM. Another case is that a quarter of MnO_6 octahedra transform to MnO_4 tetrahedra (brown rhombus) with 4*c* periodicity, including 4*c*-Tet-FM and 4*c*-Tet-AFM. For $x = 2.625$, a quarter of the MnO_6 octahedra transform to MnO_5 pentahedra, and another quarter of MnO_6 octahedra transform to MnO_4 tetrahedra, corresponding to 2*c*-T/P-FM and 2*c*-T/P-AFM. For $x = 2.5$, one half of the MnO_6 octahedra transform to MnO_4 tetrahedra, including 2*c*-Tet-FM and 2*c*-Tet-AFM order. The 2*c*-Tet-AFM phase is the BM phase mentioned above.

ELO evolution in the phase diagram

The phase diagram of LSMO oxides is predicted *via* DFT calculations (Fig. 3a, b). In the calculated LSMO system, the oxygen content (*x*) ranges from 3.0 to 2.5, and the range of in-plane strain is from −5.0% to +5.0%. The formation energy (E_f) of each phase in the same strain state is defined by the following formula:

$$E_f = E(La_{0.67}Sr_{0.33}MnO_x) - (2x-5)\cdot E(PV) - (6-2x)\cdot E(BM), \quad (2)$$

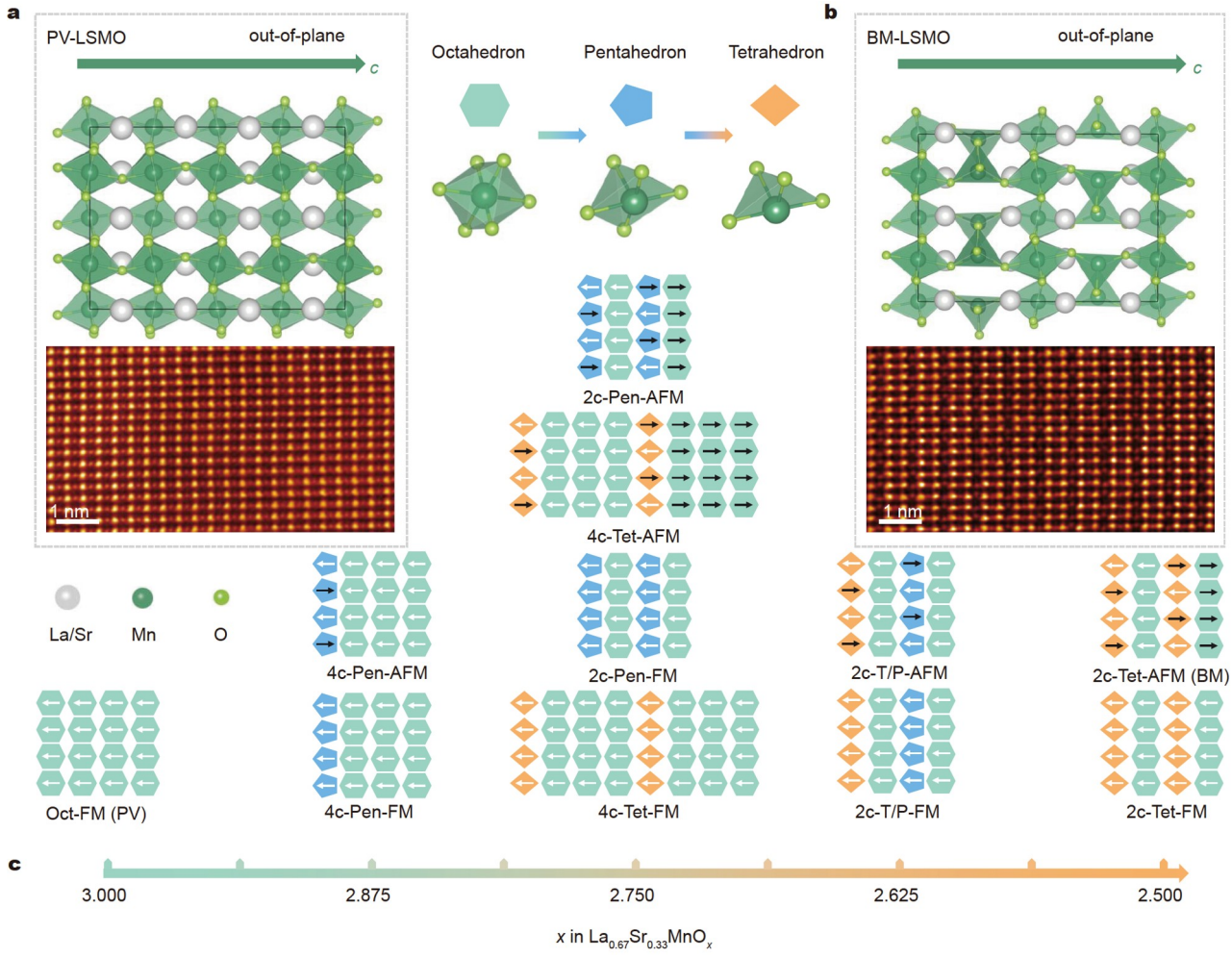

Figure 2 $La_{0.67}Sr_{0.33}MnO_x$ structures. (a, b) Structural models and HAADF images of (a) PV-LSMO and (b) BM-LSMO. (c) Schematic of phases involving oxygen ordering and Mn 3d orbital electron spin. The green hexagon denotes a MnO_6 octahedron; the blue pentagon a MnO_5 pentahedron, and the brown rhombus a MnO_4 tetrahedron. The white arrow denotes spin up and the black arrow spin down.

where x is the stoichiometric ratio of oxygen in $La_{0.67}Sr_{0.33}MnO_x$ with the range of $2.5 \leq x \leq 3.0$. The designed structures of $LSMO_x$ with x = 3.0, 2.875, 2.75, 2.625 and 2.5 are illustrated in Fig. 2c, and the corresponding atomic structures are displayed in Fig. S2. Meanwhile, we also optimize the model with random Vo (denoted as Ran-FM and only FM order is considered) for different x states, in which the initial structures are filtered by supercell software [32].

First, for the LSMO phases with 0% in-plane strain (Fig. 3a, blue symbols), the Oct-FM (PV) phase will transform to the 4c-Pen-FM phase when x decreases to 2.875 according to the formation energy, corresponding to the emergence of 4c periodic Vo stripes. In the region of $2.875 > x > 2.75$, 4c-Pen-FM and 2c-Pen-FM phases coexist, corresponding to the transformation from 4c to 2c periodicity. 2c-Pen-FM and 2c-Tet-AFM (BM) phases coexist in the region of $2.75 > x > 2.5$. The phase region is illustrated in Fig. 3b. At 2.5% tensile strain, the phase evolution trend presents an obvious difference based on the formation energy. The most stable phases are Oct-FM(PV) at x = 3.0, Ran-FM at x = 2.9375, and 2c-Tet-AFM at x = 2.5 (Fig. 3a, red symbols). The case of 5.0% tensile strain is similar (Fig. 3a, purple symbols). At −2.5% compressive strain (Fig. 3a, green symbols), the most stable phases are Oct-FM (PV) at x = 3.0, 4c-Pen-AFM at x = 2.875, 2c-Pen-FM at x = 2.75, and 2c-Tet-AFM at x = 2.5. At −5.0% compressive strain (Fig. 3a, beige symbols), the most stable phases are Oct-FM(PV) at x = 3.0, Pen-AFM at x = 2.875, T/P-AFM at x = 2.625, and Tet-AFM at x = 2.5. According to the formation energy of each phase at different strains as linked by black solid lines (Fig. 3a), strain plays an important role in the thermodynamically stable phase. The main conclusions based on the phase diagram (Fig. 3b) are as follows: (1) new phases with four-fold oxygen ordering are predicted, corresponding to the 4c-Pen-FM or 4c-Pen-AFM phase. (2) The oxygen ordered phase has priority over the disordered phase except for the initial Vo generation phase at x = 2.9375 (Fig. 3a). (3) Tensile strain favors the formation of MnO_4 tetrahedra, and compressive strain favors the formation of MnO_5 pentahedra (Fig. 3a). (4) Compressive strain favors AFM order (Fig. 3a). (5) Most stable AFM ordered phases are accompanied by MnO_4 tetrahedra, and most stable FM ordered phases are accompanied by MnO_5 pentahedra (Fig. 3a).

Fig. 3c shows that the ELO of the Oct-FM (PV) phase is {[8]d_1, [8]d_2, [8]d_3, [8]d_4, [8]d_5} at different strains. Note that the five 3d orbitals are divided into [g]d_1, [g]d_2, [g]d_3, [g]d_4, and [g]d_5 in order of energy from the lowest to the highest, where [g] represents the type of crystal field ([8], [5] or [4]) in Figs S3–S6

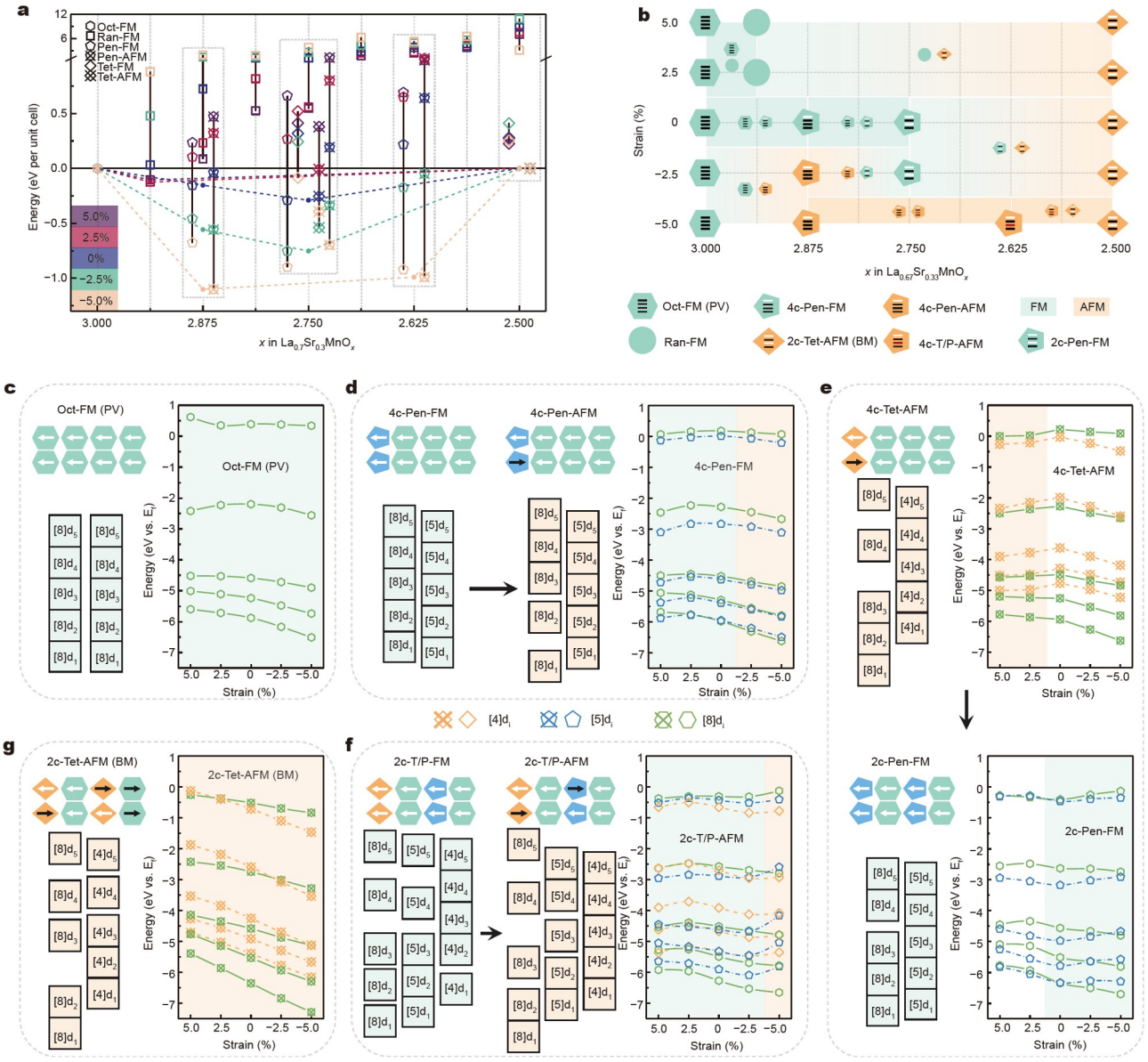

Figure 3 ELO evolution in the phase diagram. (a) Formation energies of LSMO phases with different oxygen contents (x) illustrated in Fig. 2c under different strains. Purple, red, blue, green, and beige symbols denote 5.0%, 2.5%, 0%, −2.5%, and −5% strains, respectively. (b) Phase diagram associated with the oxygen content (x) and strain. (c–g) ELO and phase transition in $La_{0.67}Sr_{0.33}MnO_x$. (c) Oct-FM (PV) phase (x = 3.0). (d) Transition from 4c-Pen-FM to 4c-Pen-AFM at x = 2.875. (e) Transition from 4c-Tet-AFM to 2c-Pen-FM at x = 2.75. (f) Transition from 2c-T/P-FM to 2c-T/P-AFM at x = 2.625. (g) 2c-Tet-AFM (BM) phase (x = 2.5). Light green and beige areas denote FM and AFM phase regions, respectively.

and Supplementary Note 1 of Supplementary information. From tensile strain to compressive strain, the splitting between orbitals obviously increases, indicating the effect of strain in orbital splitting. For x = 2.875, a quarter of the MnO_6 octahedra transform to MnO_5 pentahedra, implying changes in some of the Mn coordination environments. The ELO is {[5]d_1, [8]d_1, [5]d_2, [8]d_2, [5]d_3, [8]d_3, [5]d_4, [8]d_4, [5]d_5, [8]d_5} under tensile strain for the 4c-Pen-FM phase, corresponding to FM order (Fig. 3d). When compressive stress is applied, the degree of orbital splitting increases, and the increase for the octahedral crystal field is more severe than that for the pentahedral crystal field. This leads to a reversal of the orbitals [5]d_1 and [8]d_1, and the ELO is {[8]d_1, [5]d_1, [5]d_2, [8]d_2, [5]d_3, [8]d_3, [5]d_4, [8]d_4, [5]d_5, [8]d_5}, corresponding to AFM order. The change in ELO also gives rise to a decrease in the formation energy of the 4c-Pen-AFM phase (Fig. 3a), which becomes the dominant phase (new phase mentioned above) in the compressive strain region of the phase diagram (Fig. 3b). More importantly, the ELO in the 4c-Pen-AFM phase is consistent with that in the 4c-Pen-FM phase (Fig. S7), implying ELO is independent of the magnetic structure and corresponds one-to-one to the magnetic ground state. For the 4c-Tet phase (x = 2.75), the AFM order is more stable than the FM order, as shown in Fig. 3a. The ELO of 4c-Tet-AFM is {[8]d_1, [8]d_2, [4]d_1, [8]d_3, [4]d_2, [4]d_3, [8]d_4, [4]d_4, [4]d_5, [8]d_5}, as shown in Fig. 3e, which is generally consistent with that of 4c-Tet-FM (Fig. S8a). According to the formation energy (Fig. 3a), the 4c-Tet-AFM phase transforms into 2c-Pen-FM when the tensile strain becomes a compressive strain. The ELO at −5%

compressive strain changes to {[8]d_1, [5]d_1, [8]d_2, [5]d_2, [8]d_3, [5]d_3, [5]d_4, [8]d_4, [5]d_5, [8]d_5}, as shown in Fig. 3e. For x = 2.625 (Fig. 3f), the stable structure is the 2c-T/P-FM phase under 5%, 2.5%, 0% and −2.5% strains, the ELO of which is {[8]d_1, [5]d_1, [4]d_1, [8]d_2, [5]d_2, [4]d_2|[8]d_3|[5]d_3, [4]d_3, [5]d_4, [4]d_4, [8]d_4, [4]d_5, [5]d_5, [8]d_5}. Under −5% compressive strain, the ELO changes to {[8]d_1, [5]d_1|[8]d_2, [4]d_1, [5]d_2, [4]d_2|[8]d_3, [5]d_3, [4]d_3, [4]d_4, [8]d_4, [5]d_4, [4]d_5, [5]d_5, [8]d_5}, accompanied by the transformation from FM to AFM order (Fig. 3f). For x = 2.5 (Fig. 3g), the stable structure is the 2c-Tet-AFM phase regardless of the strain, corresponding to the ELO of {[8]d_1, [8]d_2, [4]d_1, [4]d_2, [8]d_3, [4]d_3, [8]d_4, [4]d_4, [4]d_5, [8]d_5}. Note that the order of orbitals near the Fermi energy is slightly different under different strains.

Based on the above analysis, the ELO is closely related to the stability of structural (MnO_x polyhedron) and magnetic (FM/AFM) phases, controlling the phase transition in the phase diagram of Fig. 3b. The Mn 3d_i orbital degenerate states in different crystal fields result in FM order, corresponding to an interlaced ELO. For example, the ELO of 2c-Pen-FM is {[8]d_1, [5]d_1, [8]d_2, [5]d_2, [8]d_3, [5]d_3, [5]d_4, [8]d_4, [5]d_5, [8]d_5}, in which [5]d_i and [8]d_i are close to each other. The Mn 3d_i orbital splitting states result in AFM order, corresponding to a dissociated ELO. For example, the ELO of 4c-Tet-AFM is {[8]d_1, [8]d_2, [4]d_1, [8]d_3, [4]d_2, [4]d_3, [8]d_4, [4]d_4, [4]d_5, [8]d_5}, in which [4]d_i orbitals are lifted much higher than [8]d_i orbitals. As a parameter describing the phase diagram, ELO is not only closely related to phase stability but also invariant in terms of the magnetic structure. That is, the magnetic ground state and excited state have similar ELO, which ensures the accuracy of predicting the phase diagram *via* ELO (Fig. 3c–g and Figs S7–S10).

Phase transition validation

High-quality PV-LSMO epitaxial films with a thickness of ~20 nm were deposited onto tensile (STO) and compressive (LAO) substrates using the PLD technique (see the EXPERIMENTAL SECTION for details). PV-LSMO has a rhombohedral unit cell with a pseudocubic lattice constant of 3.87 Å [36]. Thus, STO (a = 3.905 Å) and LAO (a = 3.79 Å) substrates induce tensile (0.9%) and compressive (−2.1%) epitaxial strains in the LSMO films, respectively. The structural details of the film samples are displayed in Fig. S3, Fig. S11, and Supplementary Note 2.

To verify the calculated phase diagram, we conducted STEM imaging after the specimens were annealed in the vacuum of TEM. At annealing temperatures less than 600°C, no Vo layer is observed in the film (Fig. S12). For the LSMO/STO sample, Fig. 4a–d show a set of HAADF images and the corresponding lattice spacing maps collected during the annealing process at 600°C. In the initial state (Fig. 4a), LSMO exhibits the standard PV structure. After the specimen was annealed for ~3 min at 600°C, dark stripes with 2c periodicity preferentially nucleated at the LSMO/STO interface (Fig. 4b). Note that 2c periodicity refers to an in-plane dark stripe every 2 layers. These stripes represent the oxygen-deficient MnO_4 layers and are referred to as Vo stripes [37], corresponding to the BM-LSMO phase. After ~5 min of annealing, another BM-LSMO randomly nucleated in the film (Fig. 4c) and laterally grew until the entire film was covered after ~10 min (Fig. 4d). No further change was observed in the Vo stripes at longer annealing times. This structural evolution is consistent with the results of the calculated phase diagram in Fig. 3b. The BM phase is stable under both vacuum (Fig. S13) and atmospheric conditions (Fig. S11b). A previous report [34] showed that the pristine PV-LSMO and BM-LSMO manifest FM and AFM behaviors, respectively, which is consistent with the results of the calculated phase diagram in Fig. 3b.

The dynamic behavior of Vo stripes during PV–BM transformation dramatically changed in the compressive strain (LAO) situation. Unlike the LSMO/STO case, after the LSMO/LAO heterojunction was annealed for ~3 min at 600°C, Vo stripes randomly nucleated in the whole LSMO film (Fig. 4e) and laterally grew after ~6 min (Fig. 4f). The nucleation position of Vo layers was further interpreted in Supplementary Note 3 and Fig. S14. Prior to the transformation to the BM phase, ordered Vo stripes with 4c periodicity emerged, as indicated by the small brown arrows in Fig. 4f, which correspond to an intermediate structure comprising three MnO_6 octahedral layers and one Vo layer. The coexistence of 4c and 2c periodicity (Fig. 4g) confirms the speculation of the calculated phase diagram (Fig. 3b). Fig. 4i shows enlarged HAADF image of the intermediate structure (dashed box of Fig. 4g), clearly indicating quadruple periodicity of Vo stripes. The dense diffraction points corresponding to the (00l) planes also prove the 4c periodicity (Fig. 4k and Fig. S15c), which is quasi-continuous due to the poor image quality. And this is different from the discrete diffraction points of the PV-LSMO and BM-LSMO phases (Fig. S15d, e). Finally, the BM phase continued to grow *via* splitting of the 4c periodicity into 2c periodicity and covered the entire film after ~15 min (Fig. 4h). These changes are also clearly visible in the evolution of the out-of-plane La–La distances (Fig. 4e–h), where the Vo stripes with 4c periodicity randomly nucleated, as indicated by small brown arrows, and grew toward the BM phase with 2c periodicity.

Atomic-scale observations reveal the different phase transformation responses to the in-plane strain in LSMO films. Under tensile strain (STO substrate), the PV-LSMO phase directly transforms into BM-LSMO with 2c periodicity. Based on the calculated phase diagram (Fig. 3b), the tensile strain facilitates the formation of 2c-Tet-AFM (BM) to form a two-phase coexistence between the Ran-FM and 2c-Tet-AFM (BM) phases, corresponding to the 2c periodicity observed in the STEM images (Fig. 4a–d). Under compressive strain (LAO substrate), ordered Vo stripes with 4c periodicity emerge, before the transformation to the BM phase. Then, the 4c periodicity transforms into 2c periodicity. According to the phase diagram (Fig. 3b), the 4c periodic structure contains the 4c-Pen-AFM phase with x = 2.875. Fig. 4j shows the simulated HAADF STEM image based on the calculated 4c-Pen-AFM structure, which is similar to the experimental result in Fig. 4i. The 2c periodic structures on the LAO substrate (−2.1%) likely contain the 2c-Pen-FM phase with x = 2.75, which finally transforms into the 2c-Tet-AFM (BM) phase with x = 2.5. The magnetization-temperature (M-T) curves of the LSMO film on LAO substrate (Fig. S15f) support the evolution of magnetic structures. Pristine PV-LSMO on LAO substrate characterizes with FM feature and BM-LSMO exhibits AFM behavior. The M-T curves of the 4c periodic phase are between the above two phases, corresponding to the spin reversal of partial Mn ions in the calculated 4c-Pen-AFM phase. Note that we only measured the magnetic structures of the above phases due to the difficulty of sample preparation. In general, the theoretical and experimental results agree well with each other in terms of the phase evolution trend, ensuring

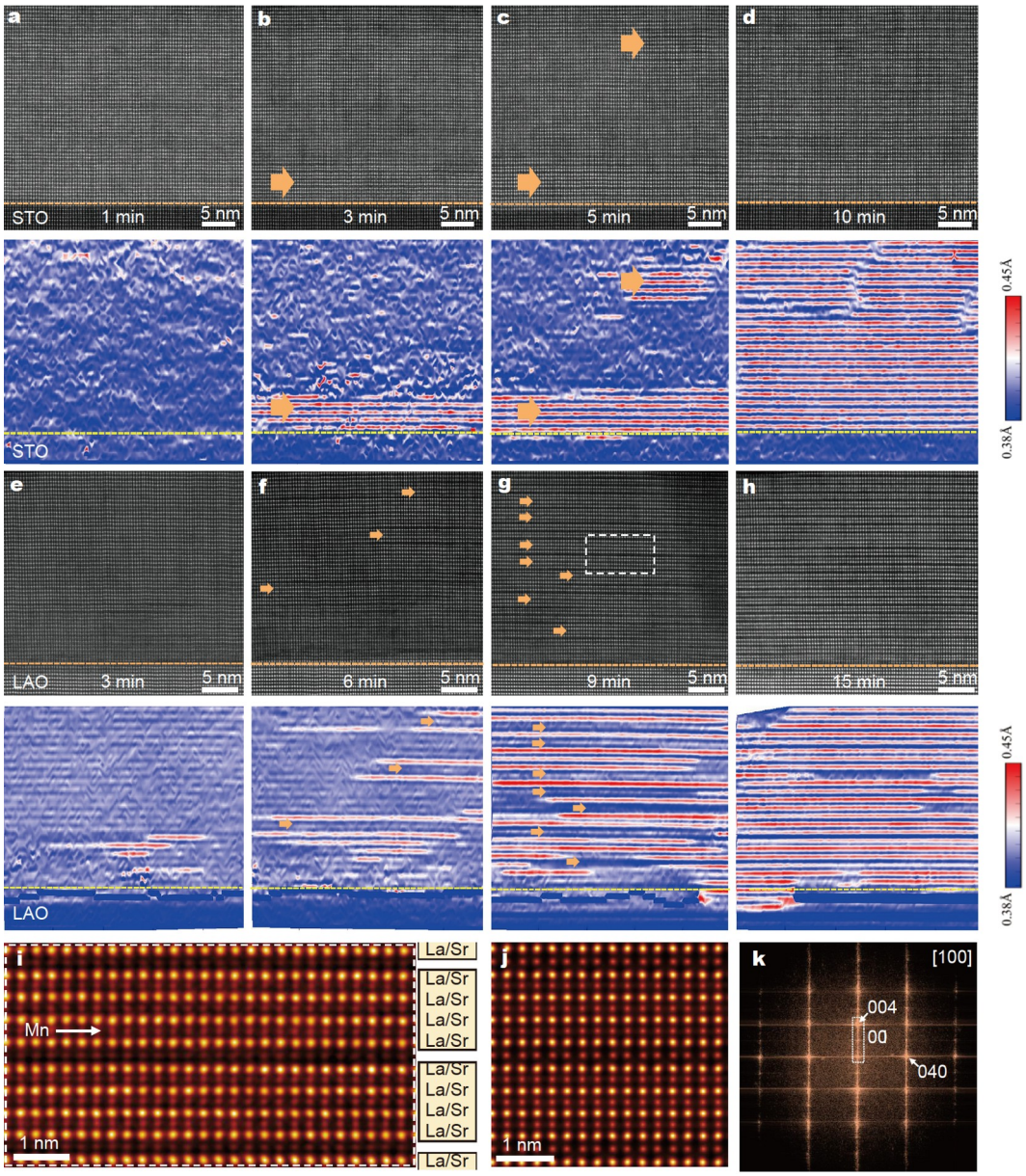

Figure 4 Structural phase evolution for tensile (STO) and compressive (LAO) substrates. Sequential STEM images of LSMO films and the corresponding out-of-plane La–La distance maps, where the Vo stripes are presented as red stripes because of the large La–La distances. (a–d) STO substrates. Brown arrows indicate the BM-LSMO phase. (e–h) LAO substrates. Small brown arrows indicate an intermediate structure with 4*c* periodicity. (i) Enlarged HAADF image of the 4*c* periodic phase in the dashed box of (g). (j) Simulated HAADF STEM image based on the calculated 4*c*-Pen-AFM structure. (k) Fast Fourier transform (FFT) pattern of (g).

the validity of the analysis for ELO evolution based on the phase diagram (Fig. 3).

Orbital elasticity law

The evolution of ELO originates from the different responses of orbital splitting to strain in different crystal fields. Qualitatively, the degree of orbital splitting is the largest and the most sensitive to strain in the octahedral crystal field (Fig. 3c–g). The orbital splitting degree and sensitivity in the pentahedral crystal field are the next largest, and those in the tetrahedral crystal field are the smallest. Thus, the combination of octahedral and tetrahedral crystal fields easily forms dissociated ELO and an AFM phase, e.g., 4*c*-Tet-AFM and 2*c*-Tet-AFM. The similar splitting energies between octahedral and pentahedral crystal fields favor interlaced ELO and an FM phase, e.g., 4*c*-Pen-FM and 2*c*-Pen-FM. Under compressive strain, the gap in the splitting energy between octahedral and pentahedral crystal fields is enlarged, leading to a change in ELO accompanied by a transformation from 4*c*-Pen-FM to 4*c*-Pen-AFM order. That is, compressive strain favors AFM order. The effect of crystal field and strain on orbital splitting can be expressed by the following equation,

$$\sigma(E) = K \cdot \Delta L, \tag{3}$$

where $\sigma(E)$ is the standard deviation of energy levels of five splitting d orbitals in a crystal field; K is the elastic coefficient of TM-d orbital splitting in a specific crystal field; ΔL is the strain that is applied in the crystal lattice.

Fig. 5a shows the linear relation between standard deviation $\sigma(E)$ and strain ΔL in octahedral crystal field in 4*c*-Pen-FM. And the elastic coefficient K is −0.92 eV Å^{-1}, implying the degree of orbital splitting decreases with the increase of strain. Similarly, the elastic coefficient K is −0.56 eV Å^{-1} in the pentahedral crystal field in 4*c*-Pen-FM, indicating the rate of decrease is less than that of the octahedron (Fig. 5b). On the contrary, the elastic coefficient K is the positive value of 0.14 eV Å^{-1} in tetrahedral crystal field in 4*c*-Tet-FM, suggesting the degree of orbital splitting rises slightly with the increase of strain (Fig. 5c). Fig. 5d shows the elastic coefficients (K) of orbital splitting in polyhedral crystal fields in these phases of Fig. 3d–g. And the graphs of linear relation between standard deviation $\sigma(E)$ and strain ΔL are displayed in Figs S16–S20. The elastic coefficient in each polyhedron is essentially the same as the results of Fig. 5a–c. An exception is that the elastic coefficient in the tetrahedron is negative in some structures. And this fluctuation may be caused by the insensitivity of the orbital splitting to stress in the tetrahedron, which is supported by the small value of elastic coefficient in the tetrahedron. The average elastic coefficients (K) of orbital splitting in octahedral, pentahedral, and tetrahedral crystal fields are −1.02, −0.37, and 0.03 eV Å^{-1} as shown in Fig. 5e. The discovery of orbital elasticity law opens up the possibility of modulating orbital splitting to control ELO.

DISCUSSION

Phase diagrams are a fundamental science, involving metallurgy, materials science, physics, chemistry, geology, and many

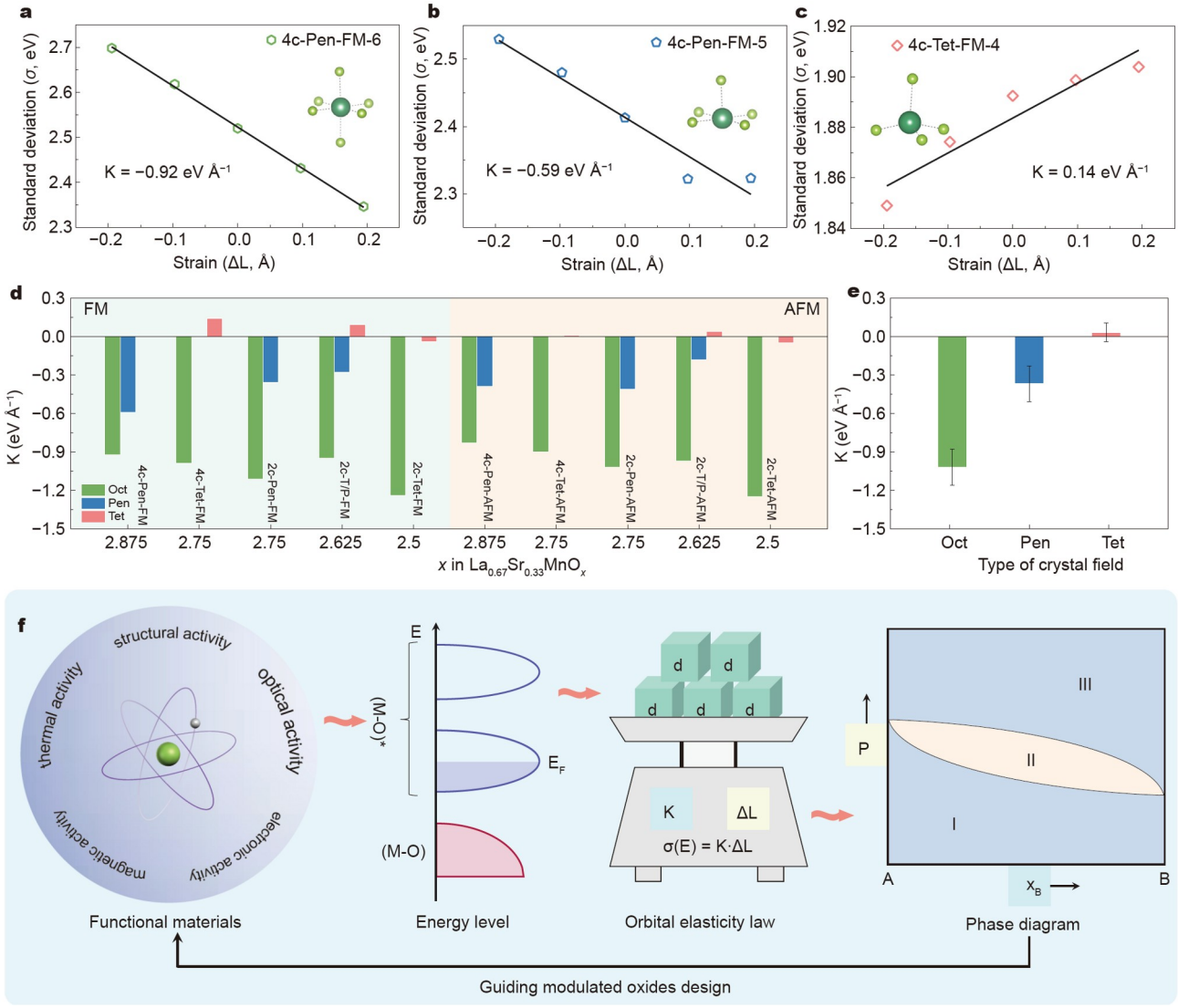

Figure 5 Orbital elasticity law and structural design of functional oxides. (a–c) Linear relation between standard deviation $\sigma(E)$ and strain ΔL in octahedral (a) and pentahedral (b) crystal fields in 4*c*-Pen-FM corresponding to $La_{0.67}Sr_{0.33}MnO_x$ with x = 2.875, and tetrahedral (c) crystal field in 4*c*-Tet-FM corresponding to $La_{0.67}Sr_{0.33}MnO_x$ with x = 2.75. (d) Elastic coefficients (K) of orbital splitting in polyhedral crystal fields in these phases of Fig. 3d–g. Light green and beige areas denote FM and AFM phase regions, respectively. (e) Average elastic coefficients (K) of orbital splitting in octahedral, pentahedral, and tetrahedral crystal fields. (f) Orbital elasticity law guides structural design of functional oxides. The first step is to determine the energy band structure of the functional material. The second is to speculate on the strain (ΔL) and elasticity coefficients ($K1$, $K2$, $K3$,…) to assemble special band structure according to orbital elasticity law. The strain corresponds to the pressure (P). And the elastic coefficients correspond to different crystal fields and TM types, indicating the composition (x_B) and framework of the system, e.g., oxygen contents and polyhedral configurations in $La_{0.67}Sr_{0.33}MnO_x$. Finally, based on the above analysis, one can predict a phase diagram for the design and discover of functional oxides with specific functionality.

industrial processes [38–40], especially which is important for the compositional design and preparation process of new materials. The structural and functional phases of phase diagram contain various kinds of ordered states, involving lattice, charge, orbital, and spin. The orbital state is a direct result of the interaction between atoms and is related to the phase stability [31]. Combining DFT calculations and experiments, the phase diagram for LSMO oxides involving the oxygen content and strain was drawn. According to the analysis and results above, the ELO plays a decisive role in the formation of phase diagram. And orbital elasticity law clarifies the origin of ELO evolution. On this basis, one can design and predict functional oxides with desirable magnetic properties. In a broader context, orbital elasticity law can enable the design and discover of functional oxides with more widely functionalities (Fig. 5f), such as structural, optical, electronic, magnetic, and thermal activities. The first step is to determine the energy band structure of the functional material. The second is to speculate on the strain (ΔL) and elasticity coefficients ($K1$, $K2$, $K3$,…) to assemble special band structure according to orbital elasticity law. The strain corresponds to the pressure (P). And the elastic coefficients correspond to different crystal fields and TM types, indicating the composition (x_B) and framework of the system, e.g., oxygen contents and polyhedral configurations in LSMO. Finally, based on the above analysis, one can predict a phase diagram for the design and discover of functional oxides with specific functionality. Orbital elasticity law broadens the means of performance modulation in the field of materials science related to ELOs.

CONCLUSIONS

In summary, combining DFT calculations and experiments, a phase diagram of LSMO oxides regarding the oxygen content and strain is built, in which the phase transition is closely related to ELO evolution. Interlaced and dissociated ELO lead to FM and AFM phases, respectively. We thereby find a new phase with four-fold oxygen ordering as a result of ELO action. Finally, the orbital elasticity law that describes the degree of orbital splitting is discovered to explain the origin of ELO evolution, with the purpose of guiding design and discover of functional oxides with specific functionality. This work defines a direction for exploring phase diagrams involving LSMO-like oxides. In a broader context, our findings open an avenue toward the development of thermodynamics and phase diagrams, laying the foundation for materials science.

Received 22 September 2023; accepted 29 November 2023; published online 17 January 2024

1 Li YS, Garst M, Schmalian J, *et al.* Elastocaloric determination of the phase diagram of Sr_2RuO_4. Nature, 2022, 607: 276–280
2 Hong SS, Gu M, Verma M, *et al.* Extreme tensile strain states in $La_{0.7}Ca_{0.3}MnO_3$ membranes. Science, 2020, 368: 71–76
3 Kapil V, Schran C, Zen A, *et al.* The first-principles phase diagram of monolayer nanoconfined water. Nature, 2022, 609: 512–516
4 Park DS, Hadad M, Riemer LM, *et al.* Induced giant piezoelectricity in centrosymmetric oxides. Science, 2022, 375: 653–657
5 Kang S, Jang WS, Morozovska AN, *et al.* Highly enhanced ferroelectricity in HfO_2-based ferroelectric thin film by light ion bombardment. Science, 2022, 376: 731–738
6 Zhang Q, Gao A, Meng F, *et al.* Near-room temperature ferromagnetic insulating state in highly distorted $LaCoO_{2.5}$ with CoO_5 square pyramids. Nat Commun, 2021, 12: 1853
7 Xiao D, Gu L. Origin of functionality for functional materials at atomic scale. Nano Sel, 2020, 1: 183–199
8 Chang YA, Chen S, Zhang F, *et al.* Phase diagram calculation: Past, present and future. Prog Mater Sci, 2004, 49: 313–345
9 Polshyn H, Zhu J, Kumar MA, *et al.* Electrical switching of magnetic order in an orbital Chern insulator. Nature, 2020, 588: 66–70
10 Li D, Lee K, Wang BY, *et al.* Superconductivity in an infinite-layer nickelate. Nature, 2019, 572: 624–627
11 Disa AS, Kumah DP, Malashevich A, *et al.* Orbital engineering in symmetry-breaking polar heterostructures. Phys Rev Lett, 2015, 114: 026801
12 Aetukuri NB, Gray AX, Drouard M, *et al.* Control of the metal–insulator transition in vanadium dioxide by modifying orbital occupancy. Nat Phys, 2013, 9: 661–666
13 Amini M, Silveira OJ, Vaňo V, *et al.* Control of molecular orbital ordering using a van der Waals monolayer ferroelectric. Adv Mater, 2023, 35: 2206456
14 Morteza Najarian A, Bayat A, McCreery RL. Orbital control of photocurrents in large area all-carbon molecular junctions. J Am Chem Soc, 2018, 140: 1900–1909
15 Gaina R, Nicholson CW, Rumo M, *et al.* Long-ranged Cu-based order with dz_2 orbital character at a $YBa_2Cu_3O_7$/manganite interface. NPJ Quantum Mater, 2021, 6: 12
16 Koohfar S, Georgescu AB, Hallsteinsen I, *et al.* Effect of strain on magnetic and orbital ordering of $LaSrCrO_3$/$LaSrMnO_3$ heterostructures. Phys Rev B, 2020, 101: 064420
17 Bristowe NC, Varignon J, Fontaine D, *et al.* Ferromagnetism induced by entangled charge and orbital orderings in ferroelectric titanate perovskites. Nat Commun, 2015, 6: 6677
18 Tokunaga Y, Lottermoser T, Lee Y, *et al.* Rotation of orbital stripes and the consequent charge-polarized state in bilayer manganites. Nat Mater, 2006, 5: 937–941
19 Singh K, Simon C, Cannuccia E, *et al.* Orbital-ordering-driven multiferroicity and magnetoelectric coupling in GeV_4S_8. Phys Rev Lett, 2014, 113: 137602
20 McMahon C, Achkar AJ, da Silva Neto EH, *et al.* Orbital symmetries of charge density wave order in $YBa_2Cu_3O_{6+x}$. Sci Adv, 2020, 6: eaay0345
21 Zhu X, Meng F, Zhang Q, *et al.* $LiMnO_2$ cathode stabilized by interfacial orbital ordering for sustainable lithium-ion batteries. Nat Sustain, 2021, 4: 392–401
22 Yao L, Inkinen S, van Dijken S. Direct observation of oxygen vacancy-driven structural and resistive phase transitions in $La_{2/3}Sr_{1/3}MnO_3$. Nat Commun, 2017, 8: 14544
23 Zhang J, Zhong Z, Guan X, *et al.* Symmetry mismatch-driven perpendicular magnetic anisotropy for perovskite/brownmillerite heterostructures. Nat Commun, 2018, 9: 1923
24 Yao L, Majumdar S, Äkäslompolo L, *et al.* Electron-beam-induced perovskite-brownmillerite-perovskite structural phase transitions in epitaxial $La_{2/3}Sr_{1/3}MnO_3$ films. Adv Mater, 2014, 26: 2789–2793
25 Kresse G, Furthmüller J. Efficient iterative schemes for *ab initio* total-energy calculations using a plane-wave basis set. Phys Rev B, 1996, 54: 11169–11186
26 Kresse G, Furthmüller J. Efficiency of *ab-initio* total energy calculations for metals and semiconductors using a plane-wave basis set. Comput Mater Sci, 1996, 6: 15–50
27 Siqi S, Jian G, Yue L, *et al.* Multi-scale computation methods: Their applications in lithium-ion battery research and development. Chin Phys B, 2016, 25: 018212
28 Blöchl PE. Projector augmented-wave method. Phys Rev B, 1994, 50: 17953–17979
29 Perdew JP, Burke K, Ernzerhof M. Generalized gradient approximation made simple]. Phys Rev Lett, 1997, 78: 1396
30 Momma K, Izumi F. VESTA 3 for three-dimensional visualization of crystal, volumetric and morphology data. J Appl Crystlogr, 2011, 44: 1272–1276
31 Khomskii DI, Streltsov SV. Orbital effects in solids: Basics, recent progress, and opportunities. Chem Rev, 2021, 121: 2992–3030
32 Okhotnikov K, Charpentier T, Cadars S. Supercell program: A combinatorial structure-generation approach for the local-level modeling of

atomic substitutions and partial occupancies in crystals. J Cheminform, 2016, 8: 17
33 Ferguson JD, Kim Y, Kourkoutis LF, *et al.* Epitaxial oxygen getter for a brownmillerite phase transformation in manganite films. Adv Mater, 2011, 23: 1226–1230
34 Cao L, Petracic O, Zakalek P, *et al.* Reversible control of physical properties *via* an oxygen-vacancy-driven topotactic transition in epitaxial $La_{0.7}Sr_{0.3}MnO_{3-\delta}$ thin films. Adv Mater, 2019, 31: 1806183
35 Moreau M, Selbach SM, Tybell T. Spatially confined spin polarization and magnetic sublattice control in (La,Sr)$MnO_{3-\delta}$ thin films by oxygen vacancy ordering. Sci Rep, 2017, 7: 4386
36 Saghayezhian M, Kouser S, Wang Z, *et al.* Atomic-scale determination of spontaneous magnetic reversal in oxide heterostructures. Proc Natl Acad Sci USA, 2019, 116: 10309–10316
37 Kim YM, He J, Biegalski MD, *et al.* Probing oxygen vacancy concentration and homogeneity in solid-oxide fuel-cell cathode materials on the subunit-cell level. Nat Mater, 2012, 11: 888–894
38 Park JH, Coy JM, Kasirga TS, *et al.* Measurement of a solid-state triple point at the metal–insulator transition in VO_2. Nature, 2013, 500: 431–434
39 Mukasa K, Matsuura K, Qiu M, *et al.* High-pressure phase diagrams of $FeSe_{1-x}Te_x$: Correlation between suppressed nematicity and enhanced superconductivity. Nat Commun, 2021, 12: 381
40 Hellwig O, Kirk TL, Kortright JB, *et al.* A new phase diagram for layered antiferromagnetic films. Nat Mater, 2003, 2: 112–116

Acknowledgements This work was supported by Beijing Natural Science Foundation (Z190010), the National Key Basic Research Program of China (2017YFA0303604 and 2019YFA0308500), the Key research projects of Frontier Science of Chinese Academy of Sciences (QYZDB-SSW-JSC035), the Youth Innovation Promotion Association of CAS (2018008), the National Natural Science Foundation of China (51672307, 51991344, 52025025, 52072400, 12074416, 12074434, and 52250402), China National Postdoctoral Program for Innovative Talents (BX20220166), and China Postdoctoral Science Foundation (2023M731863). The authors would like to thank 4B9B beamline of Beijing Synchrotron Radiation Facility (BSRF).

Author contributions Gu L, Chen L, Yu Q, and Zhang Q initiated and supervised this work. Gao A, Ji Y and Wang B designed and performed the density functional theory calculations and analyzed the data with Gu L, Chen L, Yu Q, and Zhang Q. Huang H, Du J and Liu Z grew and processed the samples under the guidance of Ge C and Jin K; Li X fabricated TEM lamellas with FIB milling; Zhang Q and Meng F performed TEM experiments and the results were analyzed by Zhang Q, Gao A, Shang T, Su D, Yu Q, Zhang Z, and Nan C; Ni H performed the magnetic and XAS experiments. Gao A and Zhang Q wrote the manuscript with valuable inputs from Yu Q, Chen L and Gu L. All authors participated in revising the manuscript.

Conflict of interest The authors declare that they have no conflict of interest.

Supplementary information Supporting data are available in the online version of the paper.

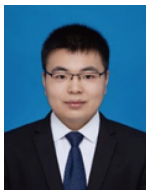

Ang Gao received his PhD degree from the Institute of Physics, Chinese Academy of Sciences, in 2022. He then worked as a postdoctoral researcher at the School of Materials Science and Engineering, Tsinghua University, under the supervision of Prof. Lin Gu. He has focused on atomic structure evolution to reveal the structure-function relationship of functional oxide materials, combining theoretical calculations and electron microscopy techniques.

Lin Gu is a professor at the School of Materials Science and Engineering, Tsinghua University, and has been engaged in the field of electron microscopy. In 2002, he graduated from Tsinghua University mentored by Academician Zhu Jing. In 2005, he received his PhD degree from Arizona State University supervised by Prof. David J. Smith. He focused on the atom and electron structure of functional oxide materials, energy storage materials and catalytic materials from lattice and charge degrees of freedom.

$La_{0.67}Sr_{0.33}MnO_3$薄膜相图的轨道弹性调控

高昂[1], 张庆华[2*], 刘倬卉[2], 孟繁琦[3], 尚彤彤[3], 尼浩[4], 黄河意[2], 杜剑宇[2], 李欣岩[2], 于搏涛[1], 苏东[2], 金奎娟[2], 葛琛[2], 吉彦舟[5], 王博[5], 余倩[6*], 张泽[6], 陈龙庆[5*], 谷林[1*], 南策文[3]

摘要 过渡金属氧化物具有丰富的功能性, 但其错综复杂的内部自由度对相图绘制和结构设计提出了挑战. 本文中, 我们引入了描述相图物理起源的轨道能级序(ELO), 并通过对$La_{0.67}Sr_{0.33}MnO_3$ (LSMO)氧化物的研究证明了其在相图预测中的有效性. 结合DFT计算和实验, 我们构建了氧含量和应变关联的LSMO相图, 结果表明LSMO结构稳定性与ELO密切相关. 据此发现了一种由ELO演化而产生的四倍氧有序相. 最后, 我们提出了描述轨道分裂程度的轨道弹性定律, 阐明了ELO演化的起源, 助力功能氧化物的设计. 这项研究拓宽了材料科学领域的性能调控手段, 并为从轨道角度预测相图提供了思路.

